Front. Chem. Sci. Eng. 2025, 19(9): 84
https://doi.org/10.1007/s11705-025-2596-4

RESEARCH ARTICLE

Non-thermal plasma driven dry reforming of methane: electron energy-input power coupling mechanism and catalyst design criteria

Minghai Shen[1,3], **Wei Guo**[1], **Lige Tong** (✉)[1], **Li Wang**[1], **Paul K. Chu** (✉)[2], **Sibudjing Kawi** (✉)[3], **Yulong Ding** (✉)[4]

1 School of Energy and Environmental Engineering, University of Science and Technology Beijing, Beijing 100083, China
2 Department of Physics, Department of Materials Science and Engineering, and Department of Biomedical Engineering, City University of Hong Kong, Hong Kong 999077, China
3 Department of Chemical and Biomolecular Engineering, National University of Singapore, Singapore 119260, Singapore
4 Birmingham Centre for Energy Storage & School of Chemical Engineering, University of Birmingham, B15 2TT, UK

Abstract Dielectric barrier discharge plasma-driven dry reforming of methane is a promising technology for syngas production. However, plasma involves complex chemical reaction pathways, non-thermal equilibrium kinetic characteristics, and interactions with catalysts, which together affect the catalytic efficiency of the dielectric-barrier plasma driven dry reforming of methane reaction and constitute its main technical challenges. This study systematically investigates the effect of critical parameters-including reactor dimensions, input power, gas flow rate, gas composition, and catalyst type-on CH_4 and CO_2 conversion as well as syngas selectivity. Through thermodynamic and kinetic analysis, we elucidate the stepwise evolution mechanism of CH_4/CO_2 reactions under low-temperature plasma conditions. Notably, we incorporated the power law relationship between electron energy and input power into the thermodynamic model, thereby quantitatively revealing for the first time the regulatory effect of input power on the reaction path. This study provides valuable design principles to enhance the efficiency and industrial applicability of dielectric-barrier plasma driven dry reforming of methane processes.

Keywords dry reforming of methane, plasma, non-thermal kinetics, nickel catalyst, thermodynamic

Received April 22, 2025; accepted June 13, 2025; online July 30, 2025

E-mails: tonglige@me.ustb.edu.cn (Tong L.),
paul.chu@cityu.edu.hk (Chu P. K.),
chekawis@nus.edu.sg (Kawi S.),
Y.Ding@bham.ac.uk (Ding Y.)

1 Introduction

Dry reforming of methane (DRM), an efficient hydrogen production method, is widely used in hydrogen production and gas synthesis. Spurred by the growing demand for energy transformation and environmental protection, methane dry reforming not only helps to optimize the utilization efficiency of natural gas resources but also provides a feasible way for the development of a low-carbon economy [1,2]. However, the traditional DRM process suffers from drawbacks such as high energy consumption, high temperature, and dependence on catalysts, consequently hampering wider industrial adoption [3−5].

Current industrial DRM technology mainly relies on high-temperature gasification, which not only has high energy consumption but also requires equipment with resistance to high temperature [6,7]. Therefore, reducing energy consumption and improving reaction efficiency are crucial to the future development of DRM. In this respect, dielectric barrier discharge (DBD) plasma-driven DRM is an emerging plasma-based catalytic reaction technology because it can efficiently excite CH_4 and CO_2 at room temperature and pressure. By using suitable catalysts, the reaction selectivity and conversion rate can be improved to potentially overcome the aforementioned hurdles [8,9].

Although DBD-DRM has been demonstrated in the laboratory, the low contact efficiency between the plasma and catalyst, low energy utilization efficiency, and complex product composition hinder further development. Simulation studies [10] have shown that in the normal

pressure DBD reaction process, electrons will split CO_2 through electron impact dissociation and produce hundreds of reactions. At present, Ni-based catalysts are one of the common catalysts in plasma DRM processes [11,12]. Although methane conversion and hydrogen production have been improved, the energy consumption and catalytic efficiency are still inferior [13,14]. The energy efficiency (E_{eff}) of CO_2 decomposition by DBD is usually less than 15% primarily because the dissociation process is dominated by electron-impact reactions, which are inherently energy-inefficient. In these non-thermal plasmas, only a small fraction of the input electrical energy is transferred to high-energy electrons capable of dissociating CO_2 molecules. Moreover, a significant portion of the energy is lost through elastic collisions, excitation of vibrational and rotational states, and other non-dissociative pathways, all of which contribute to the overall low energy utilization efficiency [15−17]. In addition, the DBD reactor design, optimization of operating conditions, and synergistic effects of plasma and catalytic reactions require improvement and better understanding to address industrial needs [18−20]. The input power directly regulates the discharge mode and the energy distribution of electrons in the plasma, thereby affecting the types and quantities of reactive species, and is the core parameter that affects the dissociation path and reaction rate of CO_2 and CH_4. The gas composition (especially the CH_4/CO_2 molar ratio) determines the relative concentration and stoichiometric balance of the reactants, and has an important influence on the composition of the syngas and the tendency of side reactions (such as carbon deposition). The gas flow rate affects the residence time of the reactants in the discharge zone, thereby affecting the degree of reaction and energy utilization efficiency. The reactor structure, especially the choice of electrode spacing, electrode material, and insulating medium, will change the discharge uniformity and plasma volume, thereby affecting the stability of the plasma and the spatial distribution of active species. In terms of catalysts, their metal components, carrier properties and metal-carrier interactions determine the surface reactivity and carbon resistance, especially in the synergistic effect of plasma and catalyst. Therefore, the optimization of the DBD-DRM system needs to comprehensively consider the above factors to achieve higher reaction selectivity, E_{eff} and catalytic stability. Among these factors, input power plays a critical role in determining the dominant reaction pathways by influencing electron energy distribution, plasma density, and the generation of reactive species. Therefore, a systematic and quantitative investigation of input power, alongside other key parameters such as reactor size, gas flow rate, gas ratio, and catalyst selection, is essential for gaining deeper insights into the reaction mechanisms and for guiding the rational design of energy-efficient DBD-DRM systems.

In the DBD-DRM process, the reaction path involves multiple endothermic and exothermic steps [21,22]. The main endothermic reaction includes the direct dissociation of CH_4 and CO_2. The exothermic step mainly involves the formation of stable products by free radical recombination. Since the DBD reaction is non-thermal plasma driven, the activation of the reactants does not depend on the overall temperature, but is driven by high-energy electrons to excite the molecules into a highly reactive state [23]. Non-thermal kinetic models are crucial in this process and can be used to describe the electron collision cross section under plasma action, electric field-driven free radical generation, reaction rate, and product distribution, providing theoretical support for optimizing the specific energy input (*SEI*), gas flow ratio, and catalyst synergy [24,25]. Although studies have clarified the coexistence of endothermic/exothermic reactions in DBD-DRM [21,22,26], the regulation mechanism of how to quantitatively correlate the electron energy distribution and *SEI* and how to inhibit and improve the efficiency of syngas production through catalyst structure design are still technical bottlenecks. Traditional thermodynamic models are difficult to describe the nonlinear relationship between electron energy and reaction rate in non-equilibrium states in DBD, and the matching mechanism between catalyst pores and plasma penetration has not yet been clarified.

This work studies the effects of various reaction parameters on the conversion rate and selectivity of DBD methane dry reforming reaction, evaluates the technical feasibility of DBD-DRM, and explores the optimization path. Based on non-equilibrium thermodynamics and kinetics analysis, the gradual evolution mechanism of the DBD-DRM reaction is discussed, and a non-thermal kinetic rate model is established to quantify the regulatory effect of input power on the reaction path. In addition, combining experimental data and model analysis, a critical pore size criterion is proposed to provide theoretical guidance for the design of efficient catalysts.

2 Experimental

2.1 Catalyst synthesis

The catalysts were prepared by the impregnation method using equal volumes of solvent. Ni-loaded γ-Al_2O_3 and Ni-loaded SiO_2 were compared to evaluate the effects of different supports. The substrate (γ-Al_2O_3/SiO_2, 100 mg, purity 99.99%) was dispersed in 25 mL of deionized water by sonication for 30 min. To load 20 wt % nickel, 0.068 mg of $Ni(NO_3)_2 \cdot 6H_2O$ (AR, purity 98%) was dissolved in 25 mL of deionized water, stirred until fully

dissolved, and then gradually added to the support solution with a 1:1 volume ratio. The mixture was stirred at room temperature for 4 h, followed by 12 h of standing to ensure complete nickel adsorption. The catalyst was washed with deionized water three times by centrifugation until pH 7 and then dried at 90 °C under vacuum for 12 h. The dried catalyst was calcined in a muffle furnace at 500 °C for 2 h with a heating rate of 1.5 °C·min^{-1} to decompose the nitrate. Prior to use, the catalyst was reduced in a 20 mL·min^{-1} H_2 atmosphere at a heating rate of 2 °C·min^{-1} to 700 °C for 2 h to ensure complete reduction of nickel oxide to nickel.

2.2 Catalyst characterization

The X-ray diffraction (XRD) patterns were collected using a BRUKER D8 ADVANCE with Cu Kα radiation (λ = 1.540598 Å), operating at 40 kV and 40 mA, with a scanning rate of 2°·min^{-1} over a 5°–90° range. Surface morphology and particle size were characterized by scanning electron microscopy (SEM) at an accelerating voltage of 10–20 kV. Mapping mode was used for element analysis, with results normalized and repeated four times. Raman scattering was conducted *in situ* using a Horiba Scientific-LabRAM HR Evolution system. UV-Vis/NIR absorption spectra were obtained with a Hitachi UH4100 spectrometer, scanning in the 200–2000 nm range. X-ray photoelectron spectroscopy (XPS) was performed using a Thermo Scientific ESCALAB 250Xi with Al Kα radiation (1487.20 eV) and calibration at 284.6 eV for the C 1s peak. The temperature distribution during the reaction was recorded using a FLIR E6xt infrared thermal imager. H_2 temperature-programmed reduction (H_2-TPR) and CO_2 temperature-programmed desorption (CO_2-TPD) experiments were carried out using a Micromeritics AutoChem 2920 chemisorption analyzer. For each measurement, approximately 100 mg of the catalyst sample was pretreated under an argon flow (40 mL·min^{-1}) at 200 °C for 1 h, followed by cooling to room temperature (25 °C). For the H_2-TPR analysis, the sample was then exposed to a 10% H_2/Ar gas mixture (40 mL·min^{-1}), and the temperature was ramped from 25 to 800 °C at a heating rate of 10 °C·min^{-1} to record the H_2 consumption profile. Similarly, for the CO_2-TPD analysis, the pretreated catalyst was cooled to 25 °C and saturated with high-purity CO_2 for 1 h. After saturation, the system was purged with argon (30 mL·min^{-1}) to remove physisorbed CO_2, followed by a temperature-programmed desorption process from 25 to 700 °C at a ramping rate of 10 °C·min^{-1} to obtain the CO_2-TPD profile.

2.3 Experimental setup

The reduced catalyst (100 mg) was mixed with γ-Al_2O_3 or quartz sand in a 1:9 ratio and ground uniformly. It was then evenly dispersed in the center of the DBD reactor, with quartz wool used to fix the catalyst layer, forming a sandwich structure. CH_4 and CO_2 were introduced as reaction gases, with He serving as the carrier gas. After 10 min of gas flow, the plasma generator (CTP-2000K, Coronalab, China) was activated and set to the specified voltage and current. After stabilization, product analysis was carried out. After dehydration using silica gel, the products were analyzed by online gas chromatography (6890A, Agilent Technologies, USA) with 3–4 measurements per sampling group. The outlet flow was measured with a soap film flow meter, and the temperature distribution during the reaction was monitored with the infrared thermal imager.

A cylindrical DBD reactor system was built, with quartz glass as the dielectric barrier material (Fig. S1, cf. Electronic Supplementary Material, ESM). Three reactor sizes were designed to study the effect of reactor dimensions on DBD discharge: small (7 mm × 2 mm × 100 mm, discharge gap 3 mm), medium (16 mm × 2.5 mm × 150 mm, discharge gap 4 mm), and large (20 mm × 2.5 mm × 150 mm, discharge gap 2 mm). For energy consumption and performance comparison, a constant input current of 1 A was used, with a discharge frequency of 7–10 kHz and input voltage ranging from 30 to 100 V, corresponding to input power levels between 30 and 100 kW. The high-voltage electrode was a stainless-steel tube at the reactor's center, with a stainless steel mesh fixed outside the quartz tube to act as the ground electrode for discharge dispersion. The discharge voltage and current signals were recorded using a Rigol DS2302A oscilloscope (China).

2.4 DBD catalysis evaluation

To evaluate the performance of DBD-DRM, the *SEI* (kJ·L^{-1}) was calculated by the following formula to reflect the effects of discharge power and total flow rate:

$$SEI = \frac{60 \times W_{\mathrm{Int}}}{Q}, \tag{1}$$

where W_{Int} is the discharge input power (W), and Q is the total flow rate (mL·min^{-1}). The conversion rate of CO_2 and CH_4 is calculated using the following formula:

$$C_{\mathrm{CO_2}} = \frac{(C_{\mathrm{CO_2}} - C_{\mathrm{CO_2,out}})}{C_{\mathrm{CO_2}}} \times 100, \tag{2}$$

$$C_{\mathrm{CH_4}} = \frac{(C_{\mathrm{CH_4}} - C_{\mathrm{CH_4,out}})}{C_{\mathrm{CH_4}}} \times 100, \tag{3}$$

where $C_{\mathrm{CO_2}}$ and $C_{\mathrm{CH_4}}$ are the CO_2 and CH_4 concentrations (mol·s^{-1}) of the inlet gas, respectively, $C_{\mathrm{CO_2,out}}$ and $C_{\mathrm{CH_4,out}}$ are the CO_2 and CH_4 concentrations (mol·s^{-1}) measured by GC, respectively. The yield (Y) and selectivity (S) of the gas product are determined by the following method:

$$Y_{H_2} = \frac{C_{H_2}}{2 \times C_{CH_4}} \times 100, \quad (4)$$

$$Y_{CO} = \frac{C_{CO}}{C_{CO_2} + C_{CH_4}} \times 100, \quad (5)$$

$$S_{H_2} = \frac{C_{H_2}}{2 \times (C_{CH_4} - C_{CH_4,out})} \times 100, \quad (6)$$

$$S_{CO} = \frac{C_{CO}}{(C_{CH_4} - C_{CH_4,out}) + (C_{CO_2} - C_{CO_2,out})} \times 100. \quad (7)$$

The carbon balance (B) of the DBD-DRM reaction process is calculated as follows:

$$B_{C_xH_y} = \frac{x \times C_{C_xH_y}}{(C_{CH_4} - C_{CH_4,out}) + (C_{CO_2} - C_{CO_2,out})} \times 100. \quad (8)$$

Among them, C_{H_2}, C_{CO} and $C_{C_xH_y}$ are the concentrations of H_2, CO, and $C_{C_xH_y}$ measured by GC ($mol \cdot s^{-1}$).

2.5 Plasma discharge calculation

Under the action of the alternating electric field, it is difficult to measure the discharge power because the phase difference between voltage and current is difficult to determine. Therefore, the voltage-charge Lissajous figure area integration method is used to determine the power of the dielectric barrier discharge. The maximum RF power and stable Lissajous figure of the oscilloscope are obtained by adjusting the discharge frequency. The input power and plasma conversion rate will also fluctuate. The actual discharge power P_{act} of DBD is calculated as follows:

$$P_{act} = \frac{1}{T}\int_0^T VI\mathrm{d}t = \frac{C_M}{T}\int_0^T V\frac{\mathrm{d}V_M}{\mathrm{d}t} = fC_M\int V\mathrm{d}V_M = fS. \quad (9)$$

In this formula: P is the discharge power (W); T is the period of the AC power supply (s); I is the loop current (A); f is the frequency of the applied voltage (Hz). S is obtained by integrating the area of the Lissajous figure.

For the E_{eff} evaluation of DBD methane dry reforming, the following calculation formula is used:

$$E_C = \frac{P_{act}}{W_{Int}} \times 100\ \%, \quad (10)$$

$$E_{eff} = \frac{C_{CO_2,con} + C_{CH_4,con}}{P_{act}} \times 100\ \%. \quad (11)$$

Among them, E_C is the energy conversion efficiency of the system, and E_{eff} is the energy yield. A measuring capacitor (C_M) is connected in series between the grounding electrode of the reactor and the ground, and the voltage across the reactor (V) and the voltage across the measuring capacitor (V_M) are collected. The two channels of the oscilloscope are connected and adjusted to the X-Y mode to obtain a closed curve, which is the Lissajous figure, as shown in Fig. S2 (cf. ESM).

3 Results and discussion

3.1 Parameters affecting the DBD reactor size

The reactor dimensions (e.g., discharge gap, diameter, and length) affect the plasma discharge characteristics and electric field distribution, consequently impacting the efficiency of generating active species, reaction rates, and product selectivity. By analyzing the effects of the reactor size, energy utilization, and methane conversion can be optimized for energy-efficient, low-consumption industrial-scale DBD reactors. Here, the performance of three DBD reactors with varying sizes is compared in Figs. 1(a)–1(c), The detailed parameters are shown in Fig. 1(d). To estimate the effective discharge volume (V_{eff}) of plasma generation in three different sizes of DBD reactors, this study adopts an approximate calculation method based on geometric parameters and discharge filling factor (f). Specifically, it is assumed that plasma is effectively generated only in part of the discharge gap, the discharge filling factor is 0.3, and the formula $V_{eff} = f \times A \times d$ is used for calculation in combination with the electrode area and spacing. The results show that the effective discharge volume of the small-sized reactor is $V_{eff} = 6.37 \times 10^{-9}$ m^3, the medium-sized reactor is 1.14×10^{-7} m^3, and the large-sized reactor is 1.06×10^{-7} m^3. These results can provide a reference basis for the analysis of energy density and plasma reaction behavior of reactors of different sizes.

As shown in Fig. 1(e), methane conversion increases from 30.96% for the small reactor to 36.29% for the large reactor. In contrast, CO_2 conversion rises slightly from 8.71% to 9.66%. This minor increase is attributed to the smaller discharge gap and optimal dielectric barrier thickness in the larger reactor, leading to more uniform and stable discharge. This improves the reaction activity and methane conversion efficiency. However, CO_2 conversion is limited by chemical equilibrium and side reactions, resulting in a smaller increase. The yields of H_2 and CO also increase significantly with reactor size. The H_2 yield rises from 9.27 to 12.54, while the CO yield increases from 4.6 to 11.32, indicating that a larger reactor provides a more stable discharge environment to facilitate methane cracking and CO_2 reactions. Higher discharge power and stable discharge characteristics also enhance the probability of reactants participating in the main reactions and reduce the occurrence of inefficient side reactions. Furthermore, the H_2 and CO selectivity increases with reactor size. The H_2 selectivity increases from 14.97% to 18.43%, while the CO selectivity rises from 6.17% to 14.06%. Meanwhile, the selectivity of by-products, such as C_2H_4, C_2H_6, and C_3H_8, decreases, particularly C_2H_4 which shows a decrease from 0.44% to 0.23%. The selectivity of C_2H_6 is very low (less than 4%), and its yield is correspondingly minor, confirming

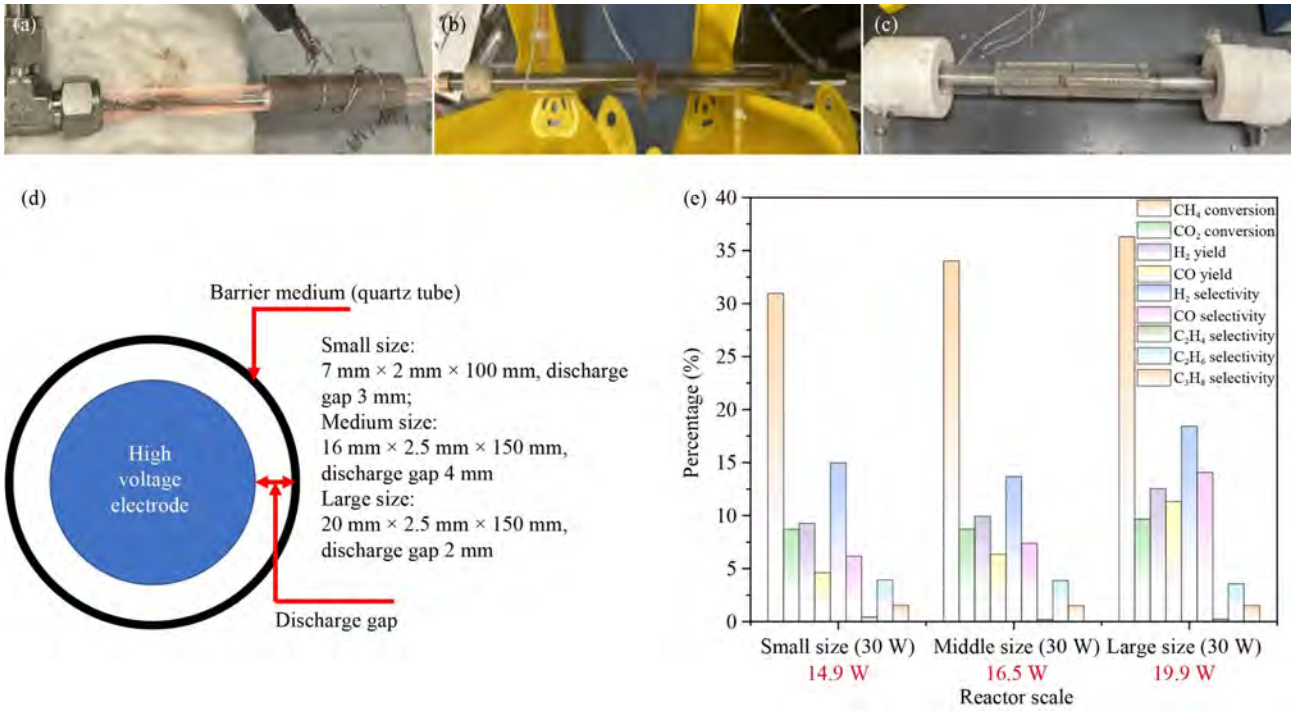

Fig. 1 Effects of different DBD reactor sizes on the catalytic activity of methane dry reforming (CH_4:CO_2 = 10:10 mL·min^{-1}): (a) small size; (b) medium size; (c) large size; (d) reactor parameters; (e) comparison of catalytic performance.

that higher hydrocarbons are not dominant products in this system. The results suggest that DBD reactors with larger effective discharge volumes and relatively smaller discharge gaps facilitate more homogeneous and volume-dominated plasma generation, which enhances the uniformity of the energy distribution within the reaction zone. The enlarged plasma-active region allows for a higher density of low-to-medium energy electrons, which are more favorable for the selective recombination of radicals into small molecular products such as CH_4 and CO_2, while minimizing excessive fragmentation and polymerization reactions that lead to the formation of complex hydrocarbons. Moreover, the reduced discharge gap strengthens the electric field, thereby promoting efficient excitation and dissociation of gas molecules at lower power inputs, contributing to improved reaction control and higher selectivity toward desired products.

Power measurements show that the small reactor operated at 14.9 and 16.5 W and the large reactor at 19.9 W, demonstrating higher discharge efficiency in the larger reactor for the same input power. This efficiency stems from that the smaller discharge gap and optimal dielectric barrier thickness contribute to more uniform and stable discharges for better efficiency. Additionally, the higher discharge power increases the average energy of electrons, thus enhancing the concentration of reactive species (such as electrons, ions, and free radicals) and promoting the main reactions. The decrease in byproduct selectivity indicates that the reaction pathway is optimized, reducing the formation of complex hydrocarbons. However, the increase in size also brings about an increase in energy requirements and an increase in design complexity.

3.2 Effects of gas flow ratio and energy input on CO_2 and CH_4 conversion efficiency

The conversion rates of CO_2 and CH_4 vary significantly for different gas flow ratios. When only CO_2 is present, the conversion rate is 17.78%, while CH_4 shows a conversion rate of 51.05%. This highlights the limited reaction efficiency of single gases, particularly CO_2, which shows lower conversion in the absence of reducing gases like CH_4. However, when CO_2 and CH_4 are introduced at flow rates of 10 mL·min^{-1} each (i.e., a CH_4:CO_2 ratio of 1:1 with a total flow rate of 20 mL·min^{-1}), the CH_4 conversion reaches 55.37%. Increasing the flow rates to 15 mL·min^{-1} each (total 30 mL·min^{-1}) further enhances the CH_4 conversion to 68.95%. However, when the flow rates increase to 20 mL·min^{-1} each (total 40 mL·min^{-1}), the conversion rates of CO_2 and CH_4 drop to 14.16% and 50.10%, respectively. This decline is likely due to overly high reactant concentrations, which lead to uneven energy distribution in the plasma zone, hinder the formation of reactive species, and promote side reactions (Fig. 2). The plasma input power in all cases was maintained at 30 W.

The introduction of He as a carrier gas alters the conversion rates of CO_2 and CH_4. Under the condition of CO_2:CH_4:He = 20:20:20, the conversion rates of CO_2 and CH_4 are 18.20% and 51.16% and are slightly higher than those without the carrier gas. When the carrier gas ratio is

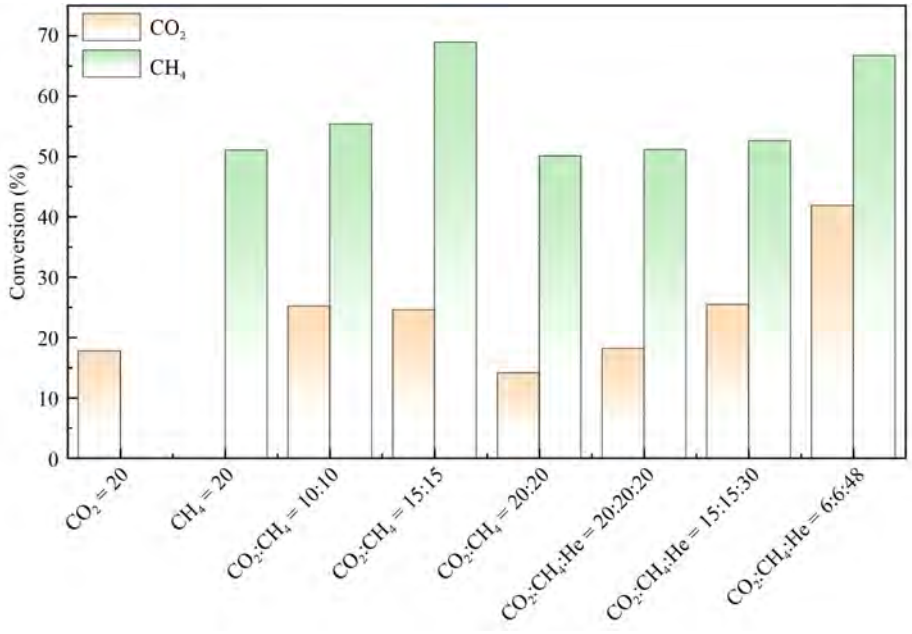

Fig. 2 Conversion rates of CH_4 and CO_2 under different CH_4:CO_2 gas compositions and inlet flow rates (10:10, 15:15, and 20:20 mL·min^{-1}). Total flow rates were 20, 30, and 40 mL·min^{-1}, respectively; input power = 30 W.

further increased (e.g., CO_2:CH_4:He = 15:15:30 or 6:6:48), the conversion rates increase significantly, with the highest conversion (41.89% and 66.75%, respectively) observed for CO_2:CH_4:He = 6:6:48. The observation suggests that He distributes the plasma energy more evenly, enhances the discharge stability, and reduce side reactions, especially under high-dilution conditions [27,28].

The optimal CO_2/CH_4 ratio maximizes the synergistic effect, and He, as a carrier gas, optimizes the reaction conditions. However, high reactant concentrations may cause energy distribution imbalances or increased side reactions to lower the conversion efficiency. The dilution effect of the carrier gas improves plasma discharge and enhances active species generation. While He can enhance discharge uniformity and reactivity in DBD systems, its practical application faces significant drawbacks. Industrially, He separation from product streams requires energy-intensive processes like membrane separation or cryogenic techniques, increasing operational costs. Additionally, its high proportion is needed to notably improve CO_2/CH_4 conversion, leading to subs tantial waste and economic inefficiency. Analytically, He interferes with H_2 detection in gas chromatography due to peak overlap, complicating yield measurements. Alternative methods—such as coupling thermal conductivity detectors with mass spectrometry or using Ar as a carrier gas—may address this, but risk higher instrument costs or reduced sensitivity. Thus, despite its plasma-enhancing properties, He's high cost, separation challenges, and analytical limitations necessitate a careful balance between performance gains and economic viability.

In large DBD reactors, the conversion rates of CH_4 and CO_2 are influenced by the *SEI* and CH_4/CO_2 feed ratio (Figs. 3(a, b)). As *SEI* increases from 90 to 240 J·mL^{-1}, both the CH_4 and CO_2 conversion rates rise. A higher *SEI* provides greater energy density, generates more active species, and enhances reaction efficiency. For a 1:1 CH_4/CO_2 feed ratio, CH_4 conversion increases from 34.66% to 61.26%, while CO_2 conversion increases from 9.05% to 21.48%. This change indicates that higher energy inputs promote the generation of energetic electrons and active species to improve reaction efficiency.

The CH_4/CO_2 feed ratio also significantly affects the conversion rates. Under high CH_4 concentrations (e.g., 4:1 and 9:1), CH_4 conversion is higher, while CO_2 conversion is lower (Fig. 3(a)). Under low *SEI* conditions, CO_2 conversion is quite low, in fact, almost zero when the CH_4/CO_2 ratio is 1:4 or 1:9, because the limited active species generated at low energy levels make CO_2 decomposition more difficult. In contrast, at lower CH_4 concentrations, the electron energy in the DBD plasma is less consumed by CH_4 dissociation and excitation processes, which typically require relatively high electron energies. As a result, more electrons remain available to activate CO_2 molecules, enhancing their conversion efficiency. Additionally, the lower CH_4 content leads to a more balanced generation of reactive species such as O•, CO, and H• radicals, and reduces the spatial and temporal fluctuation in local electron density and temperature. This results in a more uniform plasma environment across the discharge region, where energy is more evenly distributed. The improved uniformity of active species generation minimizes localized over-reduction or excessive carbon formation, thereby favoring a more selective and efficient CO_2 activation pathway

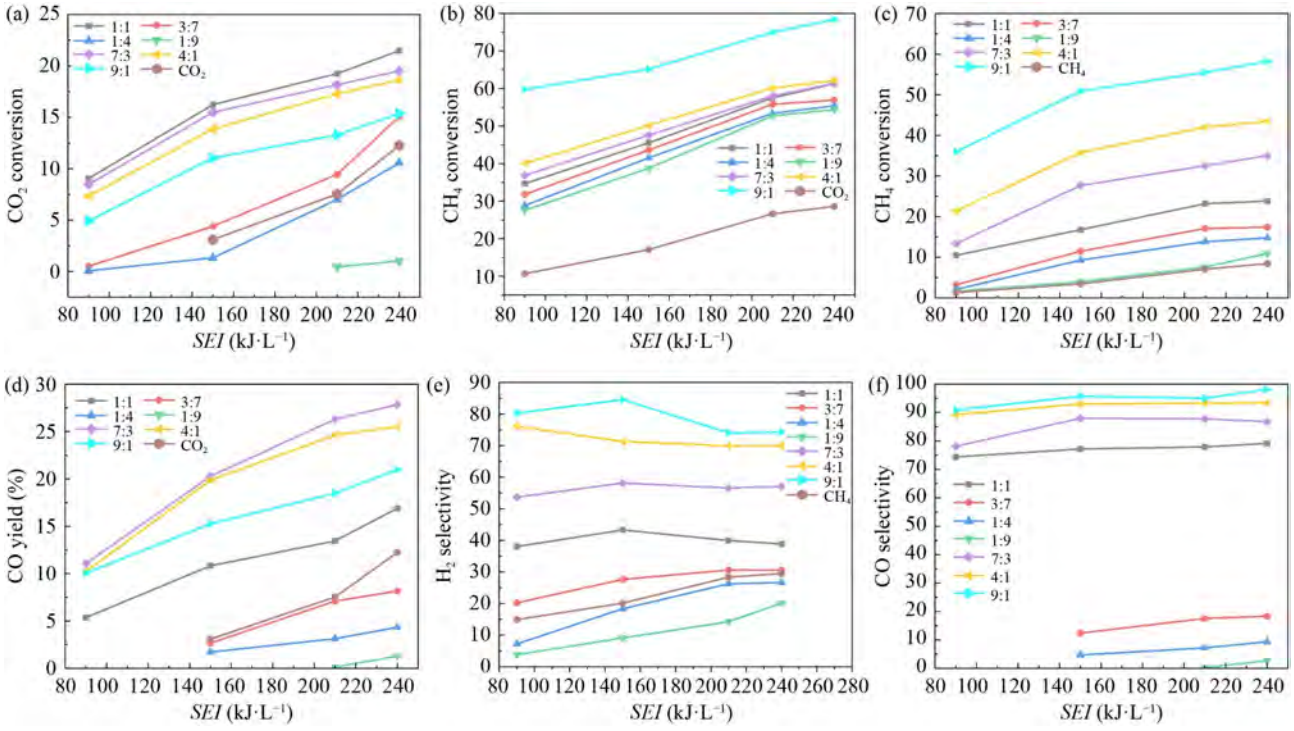

Fig. 3 Conversion rates for different CH_4/CO_2 inlet ratios (total gas flow = 30 mL·min^{-1}) with different *SEI*s: (a) CH_4, (b) CO_2, (c) H_2 yield; (d) CO yield; (e) H_2 selectivity; (f) CO selectivity.

[20,29,30]. The nonlinear characteristics of *SEI* also manifest at different feed ratios. At 240 J·mL^{-1}, CH_4 conversion significantly increases, particularly for large CH_4/CO_2 ratios (e.g., 9:1), reaching 78.38%, while CO_2 conversion is highest for a 1:1 ratio, reaching 21.48%. Under lower *SEI* conditions (e.g., 90 J·mL^{-1}), CH_4 conversion increases slowly (Fig. 3(b)), and CO_2 conversion remains low, indicating that low *SEI* limits active species generation and reduces reaction efficiency. As the energy input increases, the number of high-energy electrons and reactive species (such as O, OH, H, etc.) produced in the reactor increases, making CO_2 decomposition and related reactions (such as the reverse water gas shift reaction) more efficient.

The coupling effect of the CH_4/CO_2 ratio and *SEI* reflects the complex dynamic behavior. Under low *SEI* (90 J·mL^{-1}), high CH_4 ratios (e.g., 9:1) maintain relatively high conversion rates, suggesting that higher methane concentration promotes the collision frequency (Figs. 3(a) and 3(b)). However, under high *SEI* conditions (240 J·mL^{-1}), the conversion rate becomes more sensitive to feed ratio changes, indicating that a higher energy input enhances the responsiveness to feed ratios. Optimizing dry methane reforming requires balancing CH_4 and CO_2 conversion rates. Low CH_4/CO_2 ratios (e.g., 1:1 or 3:7) achieve reasonable conversion rates at a high *SEI*, but produce more side products, whereas high CH_4/CO_2 ratios (e.g., 9:1) increase CH_4 conversion but lower CO_2 utilization efficiency. In practical applications, adjusting *SEI*, optimizing the feed ratio, or introducing co-catalysts can improve the overall reaction efficiency.

The yield and selectivity of H_2 and CO exhibit clear trends under varying *SEI* and CH_4/CO_2 ratios. As shown in Fig. 3(c), the H_2 yield generally increases with increasing *SEI*, indicating that higher energy input promotes CH_4 activation and hydrogen production. This effect is more pronounced under CH_4-rich conditions (e.g., 4:1 and 9:1), where sufficient CH_4 provides a greater source of hydrogen-containing fragments. The maximum H_2 yield is observed at *SEI* = 240 and CH_4/CO_2 = 9:1. In contrast, at low CH_4/CO_2 ratios (e.g., 1:9), the H_2 yield remains low across all *SEI* values, especially under low *SEI*, due to limited hydrogen source and insufficient energy to effectively drive CH_4 cracking. Therefore, rather than concluding that low power input is more favorable, these results demonstrate that a combination of high CH_4 concentration and adequate *SEI* is necessary for maximizing hydrogen production via methane decomposition pathways.

The CO yield also increases with increasing *SEI*, but the magnitude is not as significant as that of H_2, as shown in Fig. 3(d). The generation of CO mainly depends on the participation of CO_2. At high CO_2 ratios (such as 1:9 and 1:4), the CO yield is high and reaches a peak in the system with CH_4/CO_2 of 7:3. On the contrary, in systems with high CH_4 content (such as 4:1 and 9:1), the CO yield is relatively low, especially when the *SEI* is low. In terms of selectivity, the selectivity of H_2 increases with the increase of *SEI*, and the improvement is more significant in systems with high CH_4 content (such as 9:1 and 4:1),

as shown in Fig. 3(e). This shows that the cracking of CH_4 plays a dominant role in the generation of H_2. When the CH_4/CO_2 ratio is 9:1, the H_2 selectivity can exceed 80%, while when the CH_4/CO_2 ratio is 1:9, the H_2 selectivity is the lowest, and even less than 10% when the *SEI* is low. The CO selectivity is closely related to the CO_2 ratio. In high CO_2 ratio systems (such as 1:9 and 1:4), the CO selectivity is high, especially close to 100% under high *SEI* conditions. In systems with high CH_4 content, the CO selectivity is significantly reduced, as shown in Fig. 3(f).

The H_2 yield increases with *SEI*, peaking at *SEI* = 240 and CH_4/CO_2 = 9:1, particularly in systems with high CH_4 ratios (e.g., 4:1, 9:1). In CO_2-deficient systems (e.g., 1:9), H_2 yield is lowest, especially for a low *SEI* (Figs. S3(a, b), cf. ESM). The CO yield also rises with *SEI* but to a lesser extent, with higher CO_2 ratios (e.g., 1:9, 1:4) promoting CO generation. The H_2 selectivity increases with *SEI*, especially in high CH_4 ratio systems, reaching over 80%, while CO selectivity is higher at high CO_2 ratios, nearing 100% under high *SEI*. The CO_2/CH_4 ratio significantly influences conversion rates, selectivity, and CO/H_2 molar ratios. CO_2 conversion increases initially and then decreases with higher CO_2/CH_4 ratios, while CH_4 conversion remains high. The CO yield peaks at a CO_2/CH_4 ratio of 2.33, and the CO/H_2 molar ratio rises with the CO_2/CH_4 ratio. A lower power favors CH_4 cracking for H_2 production.

The reaction mechanisms reveal that CH_4 cracking is key to H_2 generation ($CH_4 \rightarrow C + 2H_2$), while CO_2 reduction dominates CO production ($CO_2 + CH_4 \rightarrow 2CO + 2H_2$). A higher *SEI* accelerates both reactions to enhance the H_2 and CO yields, whereas a low *SEI* limits these reactions, especially with extreme feed ratios (Fig. S3(c)). The CO_2/CH_4 ratios play a critical role in industrial processes. Fischer-Tropsch synthesis is best for ratios of 1.5–2, methanol synthesis and syngas at 1, and ammonia synthesis requires a CO/H_2 ratio below 0.1 (Fig. S3(d)). Therefore, adjusting the feed ratios, *SEI*, and CO_2/CH_4 ratios optimizes the process for diverse industrial applications.

3.3 Effects of input power and fillers on CO_2 and CH_4 conversion rates

Both the CO_2 and CH_4 conversion rates increase with higher input power, as a higher power provides more energy to ionize and excite reactant molecules [31,32], thus enhancing plasma chemical reactions (Fig. 4(a)). In the absence of fillers, the conversion rates are relatively low due to the limited discharge region. When γ-Al_2O_3 is used as a filler, its larger surface area and excellent thermal stability promote the adsorption of reactant molecules and surface reactions, leading to a CO_2 conversion rate of 65.32%. Quartz sand, with good electrical insulation, enhances the plasma uniformity and improves both the CO_2 and CH_4 conversion rates [33]. Silica powder fares better at a low power but shows lower conversion at a high power, likely due to the adsorption of excessive intermediate products [34].

Different fillers affect the actual energy conversion rate (Fig. 4(b)) and the E_{eff}. Without fillers, the actual energy conversion rate increases with power, but E_{eff} decreases as the power increases (Fig. 4(c)). At high power, γ-Al_2O_3

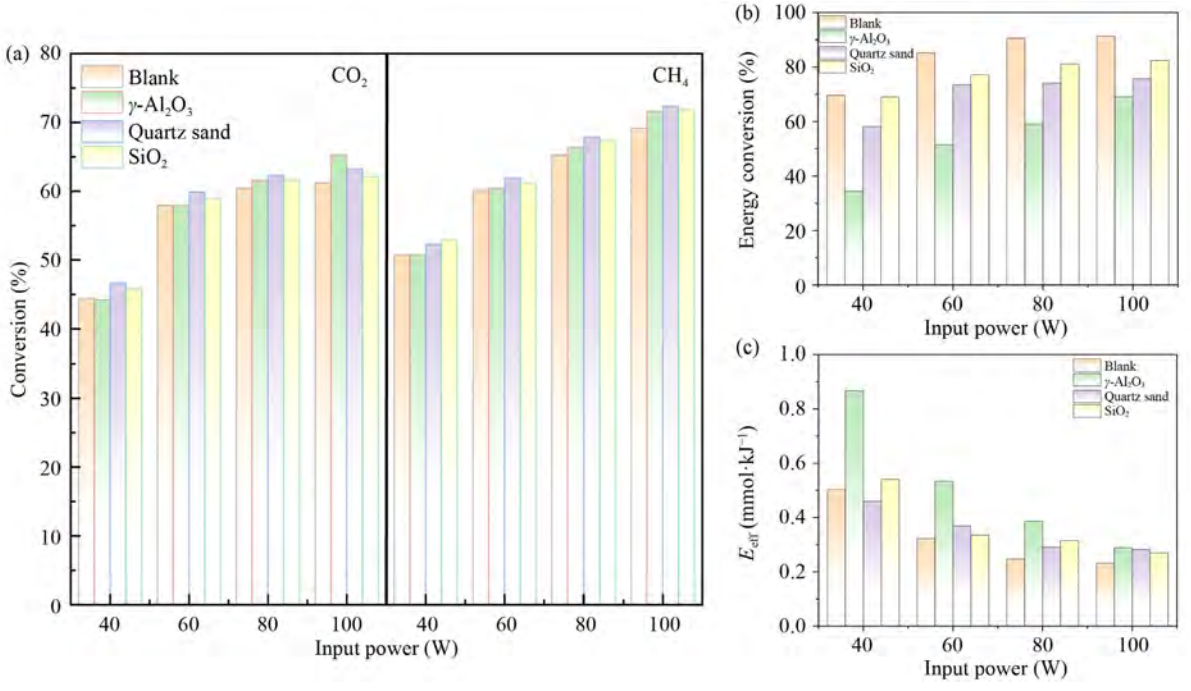

Fig. 4 Effects of different input power and different filler types: (a) CO_2 and CH_4 conversion; (b) actual energy conversion; (c) reaction energy yield.

shows a conversion rate of 69%, but E_{eff} gradually decreases with increasing power. Quartz sand maintains a stable energy conversion rate of 75.72% at 100 W, with a relatively stable E_{eff}, making it suitable for higher power applications. The electrical insulation properties and high thermal stability of quartz sand help enhance the uniformity and reaction efficiency of plasma, but its catalytic performance is relatively weak. Silica powder is better at lower power, but E_{eff} decreases at higher power, indicating reduced E_{eff}. Silica powder has a moderate specific surface area and can maintain high reactivity at low energy input. However, as the power increases, its E_{eff} gradually decreases from 0.54021 at 40 W to 0.26956 at 100 W, indicating that the marginal efficiency of energy utilization at high power is weakened.

Figure S4 (cf. ESM) shows infrared thermal images of the reactor with and without fillers at a CH_4:CO_2 feed ratio of 15:15 mL·min^{-1}. The temperature in the center of the reactor rises significantly with increasing power. After collisions between high-energy particles and gases, energy is dissipated as heat, leading to a reduction in conversion efficiency. When the high-frequency particles generated by the high-voltage electrode diffuse to the low-voltage electrode, the energy is transferred through the collision of high-concentration CO_2 and CH_4, and the energy will gradually decrease. Therefore, the e-near the center area will have lower energy and cannot further convert CO_2 and CH_4, and can only be converted in the form of heat. Due to the complex conversion process of CO_2 and CH_4 in the plasma electric field, a large number of neutral and charged particles will be generated, and this state is instantaneously stable in the electric field. However, during the mutual collision reaction, it cannot be maintained for a long time, and the reverse reaction returns to the steady-state of CO_2 and CH_4, and the remaining exothermic reactions will occur, which will be dissipated in the form of heat.

Overall, the input power and filler type influence the CO_2 and CH_4 conversion rates. Quartz sand and γ-Al_2O_3 are the best under high-power conditions, rendering them suitable for industrial applications, while silica powder is more effective under low-power conditions, making it suitable for low-energy scenarios.

3.4 Analysis of DBD-DRM reaction mechanism based on thermodynamics and kinetics

By analyzing the main endothermic and exothermic reactions of CO_2 and CH_4 decomposition in DBD [26], it was found that the plasma reaction follows a non-equilibrium mechanism and is not completely controlled by ΔH. Factors such as electron collisions and active free radicals may affect the reaction sequence. Under low electron energy (1–5.5 eV) conditions, low-energy electrons preferentially break C–H (CH_4) and C=O (CO_2) bonds through vibrational excitation (such as vibrational mode excitation of CO_2, ΔH = 0.083 eV) and direct electron collisions to generate free radicals (CH_3, H, O) and CO. The primary dissociation reactions (En1–En4) of CO_2 and CH_4 are mainly triggered by electron collisions. CO_2 dissociates through En1 and En4 to form CO and O species, while CH_4 mainly undergoes En2 and En3 reactions to break C–H bonds and generate CH_3 and H free radicals. The reaction rate at this stage is mainly controlled by the electron density (n_e) and the collision cross section (σ), and the vibration excitation mechanism plays a key role in the initial breakage of the C–H and C=O bonds. As the electron energy increases (> 12 eV), CH_4 and CO_2 are ionized (En5–En6), further forming CH_4^+ and CO_2^+. When the electron energy reaches 14–19 eV, dissociative ionization (En7–En8) occurs, producing more active charged fragments (CH_3^+, O^+, etc.), providing precursor species for subsequent exothermic recombination reactions. The following are the main endothermic and exothermic reactions of CO_2 and CH_4 in the DBD reaction (Fig. 5(a)):

(1) endothermic reactions

En1: CO_2 decomposition

$$CO_2 \rightarrow CO + 1/2O_2 \ (\Delta H = 2.93 \text{ eV})$$

En2: CH_4 electron impact dissociation

$$e^- + CH_4 \rightarrow e^- + CH_3 + H \ (\Delta H = 4.5 \text{ eV})$$

En3: CH_4 decomposition

$$CH_4 \rightarrow CH_3 + H \ (\Delta H = 4.55 \text{ eV})$$

En4: CO_2 electron impact dissociation

$$e^- + CO_2 \rightarrow e^- + CO + O \ (\Delta H = 5.5 \text{ eV})$$

En5: CH_4 electron impact ionization

$$e^- + CH_4 \rightarrow e^- + CH_4^+ + e^- \ (\Delta H = 12.6 \text{ eV})$$

En6: CO_2 electron impact ionization

$$e^- + CO_2 \rightarrow e^- + CO_2^+ + e^- \ (\Delta H = 13.8 \text{ eV})$$

En7: CH_4 electron impact dissociation ionization

$$e^- + CH_4 \rightarrow e^- + CH_3^+ + H + e^- \ (\Delta H = 14.3 \text{ eV})$$

En8: CO_2 electron impact dissociation ionization

$$e^- + CO_2 \rightarrow e^- + CO + O^+ + e^- \ (\Delta H = 19.2 \text{ eV})$$

When enough free radicals and ions accumulate, exothermic reactions (Ex1–Ex8) begin to dominate the chemical evolution of the system. Low-energy electrons (< 10 eV) promote Ex1–Ex3, that is, CO_2^+, CH_4^+, and CO^+ recombine with electrons to generate CO, O, CH_3, and H, reducing the charge density of the plasma system. In the Ex4–Ex8 reaction stage, free radical recombination becomes the dominant process, involving species such as CH_3, O, and H. H and O undergo recombination reactions (Ex6–Ex7) to form H_2 and O_2, while CO reacts with O (Ex8) to generate CO_2, which ultimately determines the

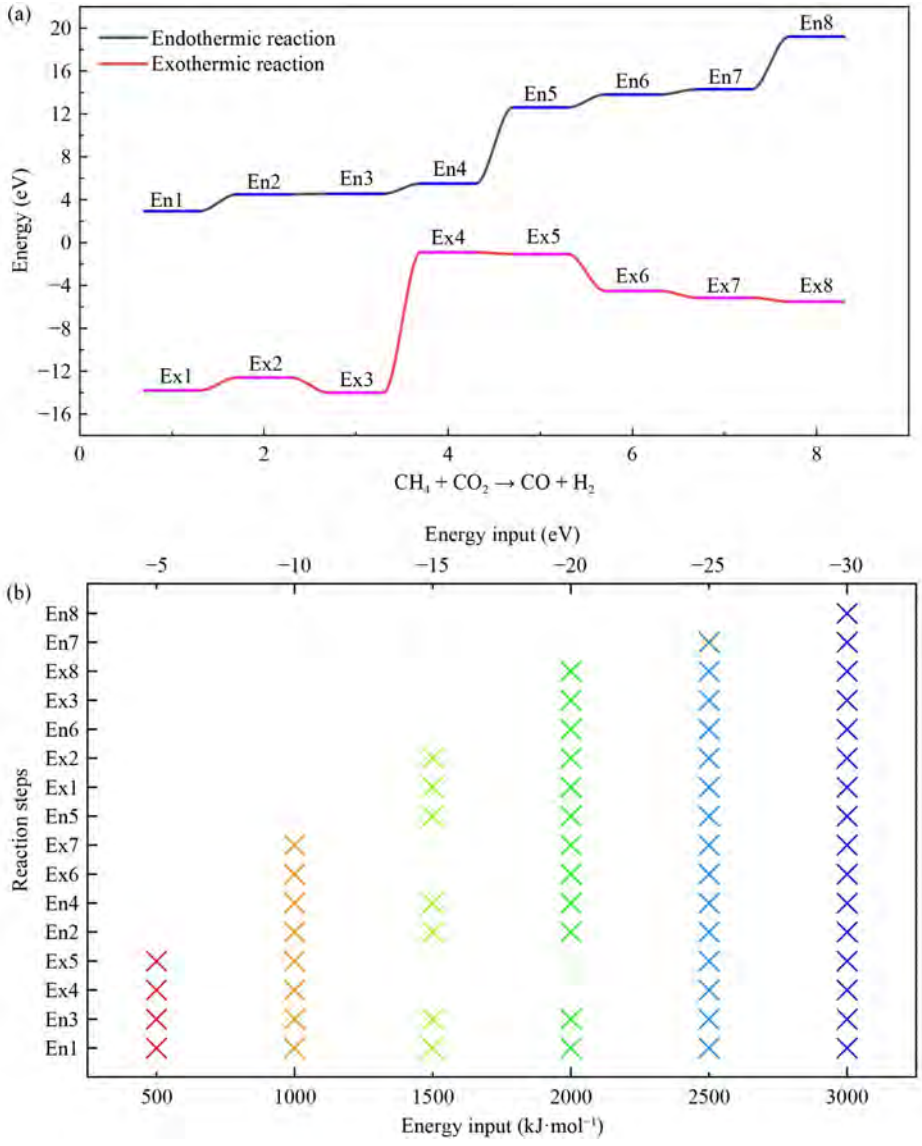

Fig. 5 (a) The main endothermic and exothermic reaction paths of CO_2 and CH_4 in the DBD reaction; (b) the reaction order under different energy inputs.

ratio of the synthesis gas (H_2/CO) product. The competition between H_2 generation (Ex6) and CO_2 reduction (Ex8) affects the selectivity of the final synthesis gas, and appropriate adjustment of the electron energy distribution helps to optimize the product ratio.

(2) Exothermic reactions

Ex1: CO_2^+ reacts with e^- to produce CO and O

$$CO_2^+ + e^- \rightarrow CO + O \ (\Delta H = -13.8 \text{ eV})$$

Ex2: CH_4^+ reacts with e^- to form CH_3 and H

$$CH_4^+ + e^- \rightarrow CH_3 + H \ (\Delta H = -12.6 \text{ eV})$$

Ex3: CO^+ reacts with e^- to produce CO

$$CO^+ + e^- \rightarrow CO \ (\Delta H = -14 \text{ eV})$$

Ex4: CH_3 reacts with CH_3 to generate C_2H_6

$$CH_3 + CH_3 \rightarrow C_2H_6 \ (\Delta H = -0.91 \text{ eV})$$

Ex5: O reacts with O_2 to generate O_3

$$O + O_2 + M \rightarrow O_3 + M \ (\Delta H = -1.09 \text{ eV})$$

Ex6: H reacts with H to produce H_2

$$H + H + M \rightarrow H_2 + M \ (\Delta H = -4.52 \text{ eV})$$

Ex7: O reacts with O to generate O_2

$$O + O + M \rightarrow O_2 + M \ (\Delta H = -5.16 \text{ eV})$$

Ex8: CO reacts with O to generate CO_2

$$CO + O \rightarrow CO_2 \ (\Delta H = -5.51 \text{ eV})$$

According to different energy inputs, considering the main triggering energy (ΔH) of CO_2 and CH_4 in the DBD reaction and their possible occurrence order in the plasma environment (Fig. 5(b)), the reaction mechanism is as follows:

(3) priority triggering of primary endothermic reaction

In a low-energy electron environment (1–5.5 eV), En1–En4 occurs preferentially:

En2: CH_4 dissociation

$$e^- + CH_4 \rightarrow e^- + CH_3 + H \ (k_1 \propto \sigma_{CH_4} n_e \sqrt{E_e})$$

En4: CO_2 dissociation

$$e^- + CO_2 \rightarrow e^- + CO + O \ (k_2 \propto \sigma_{CO_2} n_e \sqrt{E_e - 5.5})$$

Low-energy electrons break C–H (CH_4) and C=O (CO_2) bonds through vibration excitation and electron collision, generating free radicals (CH_3, H, O) and CO.

(4) Medium-high energy ionization and dissociative ionization

When the electron energy is > 12 eV, En5–En8 triggers:

En5/En6: CH_4^+/CO_2^+ ionization

$$k_{ion} = A\exp\left(-\frac{\Delta H_{ion}}{k_B T_e}\right) \ (T_e \gg T_{gas})$$

En7/En8: dissociative ionization (ΔH = 14–19 eV)

Need to be triggered by high-energy electrons (> 15 eV) to generate charged fragments (CH_3^+, O^+, etc.).

(5) Dynamic equilibrium of exothermic reactions

Exothermic reactions dominate product distribution through ion recombination and free radical recombination. After the formation of active species, exothermic reactions dominate.

Ex1–Ex3: ion-electron recombination

$$CO_2^+ + e^- \rightarrow CO + O \ (k_{rec} \propto n_e n_{ion} T_e^{-0.5})$$

Ex4–Ex8: free radical recombination

$$CH_3 + CH_3 \rightarrow C_2H_6 \ (k_{rad} \propto T_g^{-1} \exp(-E_a/k_B T_g))$$

The rates of H_2 generation (Ex6) and CO_2 regeneration (Ex8) determine the syngas (H_2/CO) ratio. The synergistic effect of endothermic and exothermic reactions in the system determines the overall energy input requirement and reaction kinetics. Low-energy electrons are mainly used for dissociation (En1–En4), medium-energy electrons (12–15 eV) promote ionization (En5–En6), and high-energy electrons (> 15 eV) trigger dissociation ionization (En7–En8). With the increase of electron temperature T_e, the ionization rate increases exponentially, while the rate of free radical recombination reaction decreases with the increase of gas temperature T_g.

Since DBD-DRM is a non-thermal reaction, the reaction rate does not fully conform to the Arrhenius formula, and it is necessary to introduce T_e to correct the rate. Fitting the electron impact rate constant k curve of CH_4 and CO_2 based on experimental data can be done by following the steps below:

Step 1: establish a kinetic model

Assuming that the main reaction path is electron impact dissociation (En2 and En4), the relationship between the reaction rate constant and the electron energy E_e is:

$$k = AE_e.$$

Among them, A is the parameter to be fitted, and E_e is related to *SEI*.

Step 2: correlate *SEI* with electron energy E_e

According to the literature [10], there is a positive correlation between the electron temperature T_e (unit: eV) and *SEI* in DBD. Assumption:

$$E_e = \alpha \times \mathrm{SEI},$$

where α is the proportional factor, which is calibrated by experimental data.

Step 3: fitting rate constant expression

I. Assuming first-order reaction kinetics:

$$X = 1 - e^{-kn_e t}.$$

Where n_e is the electron density and t is the residence time. Assuming $n_e t$ is a constant, then:

$$k \propto -\ln(1 - X).$$

II. Calculate the k_{CH_4} ratio of CH_4 (verified by experimental data in Table 1):

$$\frac{k_{240}}{k_{90}} = \frac{-\ln(1 - 0.6126)}{-\ln(1 - 0.3466)} = 2.24.$$

Combined with $k \propto E_e$ and $E_e \propto SEI$:

$$\frac{k_{240}}{k_{90}} = \sqrt{\frac{SEI_{240}}{SEI_{90}}} = 1.63.$$

The experimental ratio (2.24) is higher than the theoretical value (1.63), indicating that the effect of *SEI* on the electron density ne needs to be introduced (such as $n_e \propto SEI$), then:

$$k \propto \sqrt{E_e} \times n_e \propto \sqrt{SEI} \times SEI = SEI^{1.5}.$$

The corrected ratio is:

$$\frac{k_{240}}{k_{90}} = \left(\frac{240}{90}\right)^{1.5} \approx 2.24$$

(consistent with experimental values).

Therefore, the rate constant expression is:

$$k_{CH_4} = A \times SEI^{1.5}.$$

Step 4: determine parameter A

Using data when *SEI* = 90 J·mL^{-1}:

$$0.3466 = 1 - e^{-kn_e t} \Rightarrow kn_e t \approx 0.425.$$

Assume $n_e t = B \cdot SEI$ (because $n_e \propto SEI$), then:

$$k = A \times SEI^{1.5} \Rightarrow 0.425 = A \times 90^{1.5} \times B \times 90.$$

It needs to be solved in conjunction with CO_2 data, but

Table 1 Relationship between CH_4/CO_2 conversion rate and input energy ratio

SEI (J·mL^{-1})	CH_4 conversion rate (%)	CO_2 conversion rate (%)
90	34.66	9.05
150	45.52596	16.22196
210	57.50994	19.24503
240	61.26	21.48

for simplicity, A is calibrated directly:

$$A_{CH_4} = \frac{0.425}{90^{2.5}} \approx 6.2 \times 10^{-6}\ \mathrm{cm^3 \cdot s^{-1} \cdot J^{-1.5}}.$$

Similarly, a similar fitting is performed on the CO_2 conversion rate to obtain:

$$A_{CO_2} \approx 2.1 \times 10^{-6}\ \mathrm{cm^3 \cdot s^{-1} \cdot J^{-1.5}}.$$

Step 5: verify consistency with the literature

Combined with the electron collision cross section of CO_2 in the literature [15] ($\sigma_{CO_2} = 3.2 \times 10^{-16}$ cm^2@ E_e = 6 eV):

$$k = \sigma \times v_e \times n_e = \sigma \times \sqrt{\frac{2eE_e}{n_e}}.$$

Substitute E_e = 6 eV, $n_e = 10^{10}$ cm^{-3} (typical DBD value):

$$k_{CO_2} \approx 3.2 \times 10^{-16} \times 9.5 \times 10^7 \times 10^{10} = 3.0 \times 10^{-3}\ \mathrm{cm^3 \cdot s^{-1}}.$$

This is consistent with the fitting result ($A_{CO_2} \times 240^{1.5} \approx 2.1 \times 10^{-6} \times 240^{1.5} \approx 0.008\ \mathrm{cm^3 \cdot s^{-1}}$).

$$k_{CH_4} = 6.2 \times 10^{-6} \times SEI^{1.5}, k_{CO_2} = 2.1 \times 10^{-6} \cdot SEI^{1.5}.$$

The reaction rate constant ($k \propto SEI^{1.5}$) shows that the electron energy distribution and collision frequency affected by electron density (n_e) and T_e regulate the reaction efficiency through *SEI*. When *SEI* increases from 90 to 240 J·mL^{-1}, n_e and E_e increase simultaneously, significantly improving the CH_4 conversion rate (34.66% → 61.26%).

As *SEI* increases, T_e shows an upward trend, but the growth rate gradually slows down. At lower *SEI* (< 150 J·mL^{-1}), the electron temperature is low and the plasma reaction activity is limited (Fig. 6). After *SEI* exceeds 180 J·mL^{-1}, T_e growth slows down, indicating that the electron energy may be close to the saturation value. The power increase may not significantly improve the methane conversion rate, but may promote side reactions (such as CO_2 excessive dissociation). The selection of a suitable *SEI* requires a balance between the electron temperature and the target reaction activity to avoid unnecessary energy loss and by-product generation. Therefore, precise control of the electron energy distribution and the gas phase temperature T_g is of great significance for optimizing the CH_4/CO_2 conversion reaction.

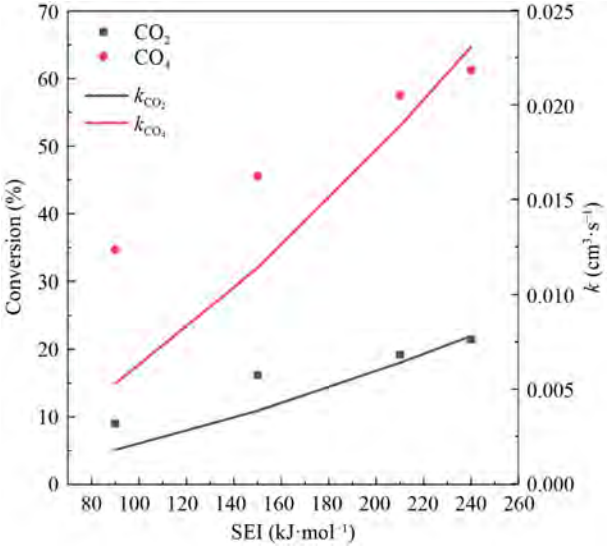

Fig. 6 The electron collision rate and conversion rate of CO_2 and CH_4 in DBD-DRM reaction vary with *SEI*.

3.5 Ni-based catalysts in DBD-DRM

To investigate the performance and reaction mechanisms of Ni-based catalysts in DBD-DRM, 20 wt % Ni@γ-Al_2O_3 and 20 wt % Ni@SiO_2 are synthesized. The choice of 20 wt % Ni loading is based on a survey of previous studies, where Ni loadings in the range of 10–30 wt % have been commonly employed for plasma-assisted dry reforming of methane. Among them, 20 wt % Ni is widely reported to offer a good balance between metal dispersion, catalytic activity, and resistance to sintering under plasma conditions [35–37]. Moreover, the purpose of this study is not to develop novel catalysts, but to evaluate the kinetic behavior and plasma–catalyst interaction of representative and conventional Ni-based catalysts. Therefore, selecting a typical and well-studied loading such as 20 wt % enhances the comparability and reproducibility of the results, while providing a stable benchmark for investigating the effects of plasma parameters. The particle sizes of the catalysts vary, with γ-Al_2O_3 exhibiting a more uniform nanostructure (Figs. 7(a) and 7(b)). The actual Ni loading on SiO_2 slightly exceeds the expected 20 wt %, as confirmed by EDS (Figs. 7(c) and 7(d)). XRD shows that Ni is evenly distributed in both catalysts, without forming large crystalline particles and indicating a uniform atomic dispersion of Ni (Fig. 7(e)). Raman scattering confirms no phase transformation of Ni, with characteristic peaks corresponding to Si–O and Al–O vibrations at 504 and 375 cm^{-1}, respectively (Fig. 7(f)). This light primarily includes ultraviolet (UV), visible (Vis), and near-infrared (NIR) radiation, with wavelengths typically ranging from 100 to 3000 nm (Fig. 7(g)). The specific wavelength range varies depending on factors such as the type of plasma, discharge power, and gas composition. UV light enhances reaction activity by exciting reactant molecules and influencing the optical properties of the catalyst. Visible light improves catalytic activity through surface plasmon resonance effects. NIR light manifests as thermal energy, suggesting that plasma discharge processes may facilitate light-assisted catalytic reactions. XPS reveals that Ni on SiO_2 has predominantly a higher oxidation state, indicating strong electronic interaction between Ni and SiO_2 and likely formation of NiO or Ni-Si-O compounds (Figs. 7(h)–7(k)). In contrast, Ni on γ-

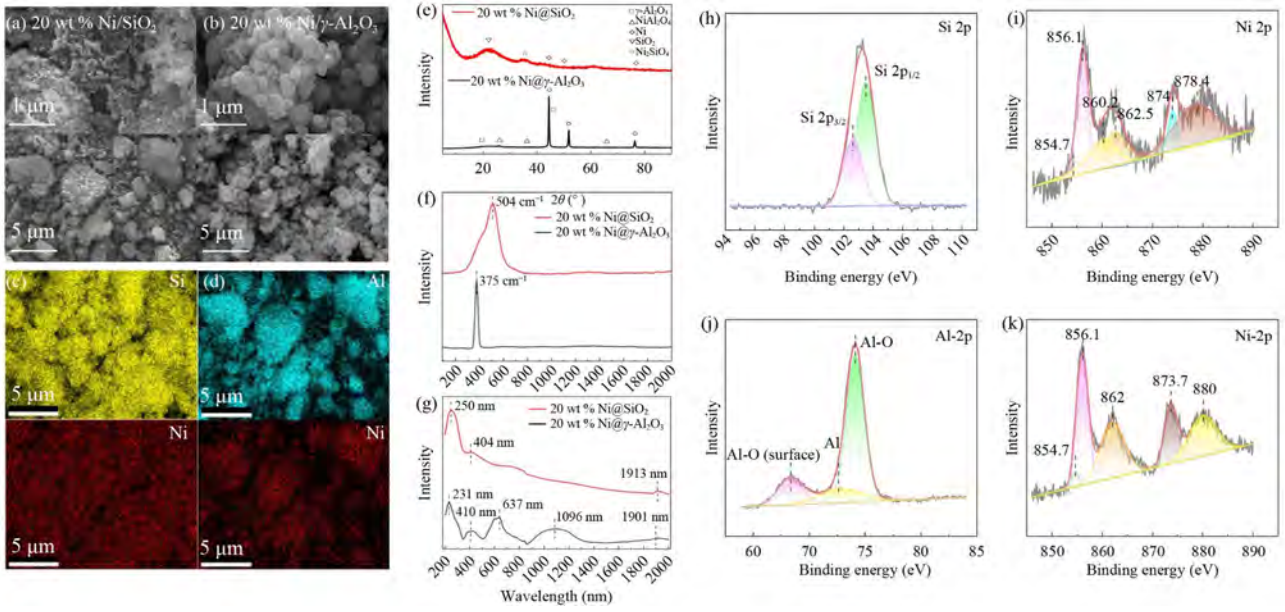

Fig. 7 SEM images of (a) 20 wt % Ni@γ-Al_2O_3 and (b) 20 wt % Ni@SiO_2; EDS spectra: (c) 20 wt % Ni@γ-Al_2O_3 and (d) 20 wt % Ni@SiO_2; (e) XRD spectra of 20 wt % Ni on different substrates; (f) Raman scattering spectra of 20 wt % Ni@γ-Al_2O_3 and 20 wt % Ni@SiO_2 catalysts; (g) UV-Vis absorption spectrum; XPS spectra of 20 wt % Ni on different substrates: (h) Si 2p and (i) Ni 2p on SiO_2; (j) Al 2p and (k) Ni 2p on γ-Al_2O_3.

Al_2O_3 exhibits a more complex chemical state, including both metallic Ni and Ni^{2+}. The excitation and dissociation processes between electrons and gas molecules within the plasma generate electromagnetic radiation, resulting in a glow.

The H_2-TPR profiles of the fresh catalysts are shown in Fig. 8(a). For the Ni@Al_2O_3 catalyst, two distinct hydrogen consumption peaks were observed at approximately 440 and 601 °C. The first peak can be attributed to the reduction of bulk NiO species that are weakly interacting with the Al_2O_3 support, while the second peak corresponds to the reduction of NiO species moderately interacting with the Al_2O_3 support. Notably, no high-temperature reduction peak was detected above 700 °C, suggesting that the formation of the strongly bound $NiAl_2O_4$ spinel phase is negligible under the applied preparation and calcination conditions. This indicates that NiO is the dominant Ni species present in Ni@Al_2O_3, and the metal-support interaction is moderate. In comparison, the H_2-TPR profile of the Ni@SiO_2 catalyst exhibited a single broad reduction peak centered at approximately 500 °C. This high-temperature peak can be ascribed to the reduction of NiO species confined within the porous SiO_2 framework or the formation of highly dispersed nickel silicate-like species, which are more difficult to reduce due to strong metal–support interactions and potential structural incorporation. The absence of a low-temperature peak suggests that weakly bound or bulk-like NiO is scarce in Ni@SiO_2, possibly due to strong dispersion or encapsulation of Ni species within the silica matrix. Clearly, the reduction temperature of Ni@Al_2O_3 is more distributed, with a noticeable fraction of NiO reducible at lower temperatures (440 °C), implying the existence of more easily reducible Ni species. In contrast, the single, higher-temperature peak in Ni@SiO_2 reflects a more uniform but strongly bound

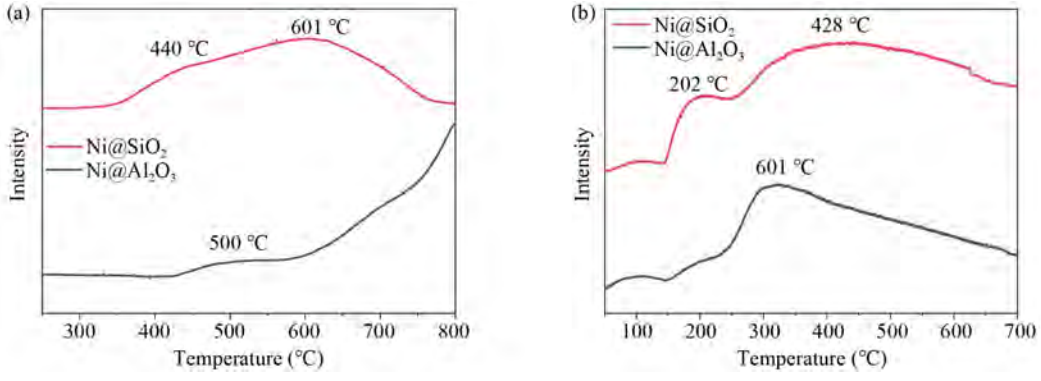

Fig. 8 (a) H_2-TPR profiles of 20 wt % Ni@γ-Al_2O_3 and 20 wt % Ni@SiO_2; (b) CO_2-TPD profiles of 20 wt % Ni@γ-Al_2O_3 and 20 wt % Ni@SiO_2.

NiO phase. This indicates that Ni@Al_2O_3 has relatively better reducibility than Ni@SiO_2 under comparable conditions, which may lead to a higher fraction of active metallic Ni species being generated at moderate activation temperatures. Therefore, the support type plays a critical role in determining the reducibility of the Ni species. The Al_2O_3-supported Ni catalyst exhibited enhanced hydrogen activation and more favorable reduction characteristics compared to the SiO_2-supported counterpart. This difference may influence subsequent catalytic performance, especially in reactions where the generation of metallic Ni at lower temperatures is essential.

The CO_2-TPD profiles of Ni@Al_2O_3 and Ni@SiO_2 catalysts were analyzed to assess their CO_2 absorption capabilities, as illustrated in Fig. 8(b). For Ni@SiO_2, the desorption peak observed at 202 °C corresponds to weak basic sites on the catalyst surface, while the peak at 428 °C is attributed to sites with moderate basicity. In contrast, Ni@Al_2O_3 exhibits a desorption peak at 601 °C, indicative of strong basic sites. The presence of strong basic sites in Ni@Al_2O_3 suggests a higher capacity for CO_2 chemisorption and dissociation compared to Ni@SiO_2, which primarily features weaker and moderately basic sites. This difference implies that Ni@Al_2O_3 would likely demonstrate superior performance in CO_2 conversion and methane activation due to its enhanced ability to adsorb and dissociate CO_2. Furthermore, the strong basic sites on Ni@Al_2O_3 can provide additional surface oxygen, improving the catalyst's resistance to carbon deposition. In summary, the basicity and CO_2 absorption ability of the catalysts follow the sequence Ni@Al_2O_3 > Ni@SiO_2, with Ni@Al_2O_3 being more effective for reactions involving CO_2 due to its strong basic sites.

The catalytic performance of both catalysts increases with input power (Fig. 9(a)). At 100 W, 20 wt % Ni@SiO_2 exhibits a slightly higher CO_2 conversion rate (25.36%) compared to 20 wt % Ni@γ-Al_2O_3 (21.78%), possibly due to enhanced exposure of active sites on SiO_2 at high power. At 40 W, the difference in conversion rates between the two catalysts is minimal, indicating limited activation of active sites. Similarly, the CH_4 conversion rate increases with power, with 20 wt % Ni@SiO_2 showing slightly higher conversion at 100 W (62.55%) compared to 20 wt % Ni@γ-Al_2O_3 (62.05%), likely due to the better dispersion of Ni particles and more uniform distribution of active sites on SiO_2.

The production rates of H_2 and CO exhibit different trends. At 40 W, the H_2 yield from 20 wt % Ni@γ-Al_2O_3 is slightly higher, but as power increases, the yields of both catalysts approach each other (Fig. 9(b)). Notably, the CO yield of 20 wt % Ni@SiO_2 is higher than that of 20 wt % Ni@γ-Al_2O_3 under all power conditions, espe-

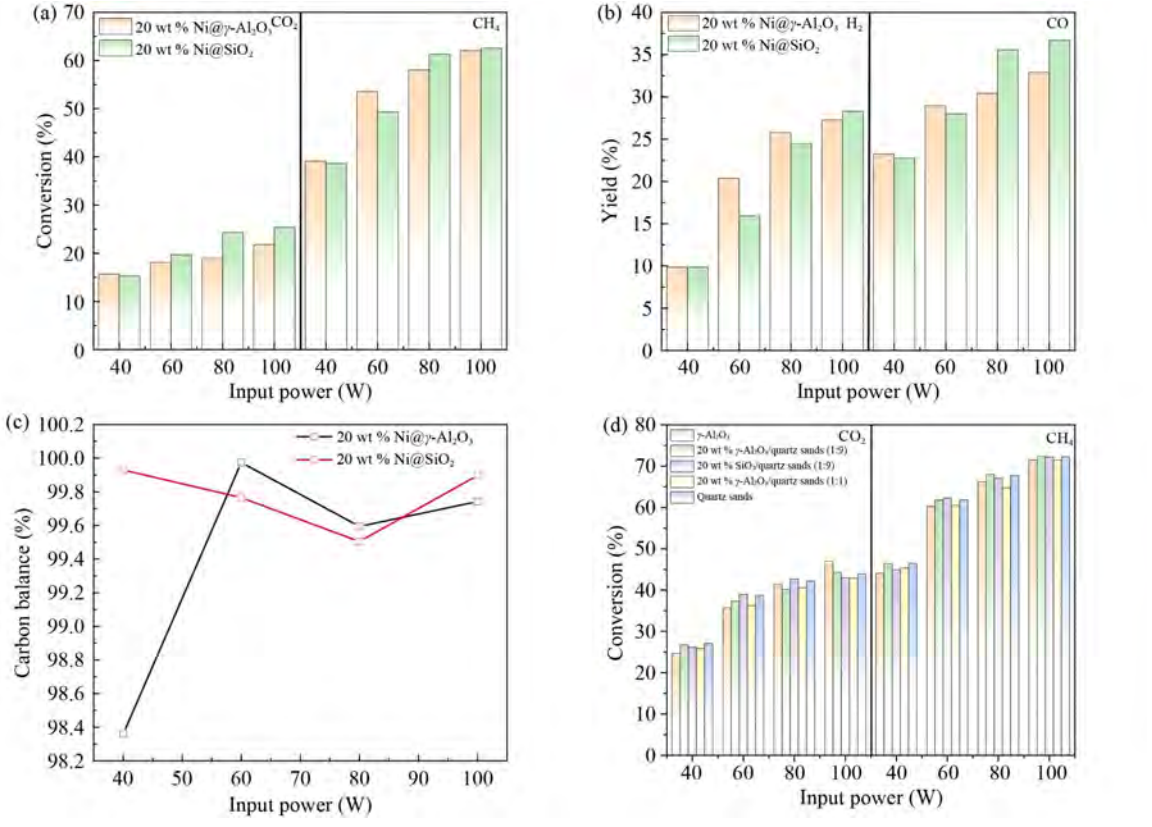

Fig. 9 Ni-based catalysts at different input powers: (a) CO_2 and CH_4 conversion; (b) H_2 and CO yields; (c) carbon balance; (d) the effect of the mixing ratio with the carrier on CO_2 and CH_4 conversion.

cially 100 W because the neutral surface characteristics of SiO_2 suppresses the water-gas shift reaction, leading to higher CO retention. 20 wt % Ni@SiO_2 exhibits slightly better selectivity for H_2 and CO at high power, while 20 wt % Ni@γ-Al_2O_3 shows higher selectivity for hydrocarbon byproducts (such as C_2H_4, C_2H_6, and C_3H_8) (Figs. S4(a, b), cf. ESM). This may be because the basic surface sites on γ-Al_2O_3 promote hydrocarbon polymerization. Both catalysts maintain a high carbon balance close to 99%–100% (Fig. 9(c)), indicating minimal carbon loss and high system efficiency during DBD-DRM. The carbon balance of 20 wt % Ni@SiO_2 is slightly higher than that of 20 wt % Ni@γ-Al_2O_3, suggesting better suppression of side reactions, particularly coke formation. However, a closer examination of the data reveals subtle but consistent differences. For instance, at a CH_4/CO_2 ratio of 40, the carbon balance of 20 wt % Ni@γ-Al_2O_3 is 98.36%, noticeably lower than the 99.93% observed for 20 wt % Ni@SiO_2. Although the carbon balance of Ni@γ-Al_2O_3 improves at higher ratios (e.g., up to 99.74% at 100), the values remain slightly lower overall compared to Ni@SiO_2 across all test points. These results suggest that Ni@SiO_2 exhibits better suppression of carbon loss pathways, likely due to its weaker surface basicity, which reduces hydrocarbon polymerization and subsequent coke formation. In contrast, the stronger basicity of γ-Al_2O_3 may favor C–C coupling reactions and polymer growth, leading to minor but measurable carbon retention on the catalyst or reactor surfaces. Therefore, while both catalysts perform well in maintaining a high carbon balance, Ni@SiO_2 shows slightly superior control over side reactions, which may be advantageous for long-term plasma-catalytic DRM applications.

Under reaction conditions of CO_2:CH_4:He = 6:6:48, both the CO_2 and CH_4 conversion rates increase with power. At low power, the catalytic effect of the active metal is more pronounced, while at higher power, the physical properties of the substrate have a greater influence on the reaction efficiency (Fig. 9(d)). As the power increases from 40 to 100 W, the conversion rates of all the catalyst-substrate combinations improve due to enhanced plasma activation, which produces better excitation and decomposition of reactant molecules.

The differences between catalysts and substrates are significant. When using quartz sand alone, the conversion rates at high power are similar to those of the mixed systems. Particularly at 80 and 100 W, quartz sand delivers excellent performance, likely due to its high-temperature stability and large surface area. When mixed with 20 wt % Ni@γ-Al_2O_3, quartz sand dominates the reaction at higher power, diluting the activity of the Ni-based catalyst [11]. In contrast, the combination of 20 wt % Ni@SiO_2 and quartz sand shows optimal results at 60 and 80 W, suggesting that the SiO_2 substrate facilitates the uniform distribution of metal particles and efficient utilization of active sites. Using γ-Al_2O_3 alone results in the lowest conversion rate at low power, but at high power, its performance approaches that of other mixed systems, indicating that plasma activation can compensate at lower power. The results show that different catalyst-substrate combinations are suitable for different power conditions, with the dispersion of the catalyst and the material properties of the substrate playing key roles in the conversion rates, especially at low input power.

This study shows that different catalyst and substrate combinations are suitable for different power conditions. Under high power conditions, since the catalytic reaction of DBD is close to the thermodynamic limit, Ni-based catalysts have little effect on improving the conversion rate. On the contrary, an efficient substrate, such as quartz sand, can improve the discharge effect. Under low power conditions, due to the limited input energy, the dispersion of metal catalysts and the selection of substrate both affect the improvement of reaction efficiency. Combined with the analysis of energy conversion rate and E_{eff}, in order to reduce the energy consumption of DBD reactors, future research on high CO_2 and CH_4 conversion rates under low input power mode should focus on the dispersion of catalysts and the material properties of carriers.

To clarify, the primary objective of this study is to investigate the catalytic performance and reaction behavior of conventional Ni-based catalysts under DBD-assisted dry reforming conditions, with a focus on the effects of discharge parameters, gas composition, and catalyst type on conversion efficiency and product distribution. Although catalyst stability is an important parameter for practical application, the current reactor configuration imposes certain limitations for long-duration testing. Specifically, under extended operation (beyond 10 h), localized hotspots caused by plasma–catalyst interactions may lead to gradual temperature rise, catalyst fouling, and the formation of condensed organic residues on the reactor wall or electrode surface, which ultimately affect discharge uniformity and reaction reliability.

Given these constraints, this work does not include long-term durability studies. Instead, it emphasizes short-term performance trends and mechanistic insights under varying process conditions. In future research, we plan to optimize the DBD reactor design and its thermal management system to enable extended, stable plasma-catalytic operation and allow for comprehensive lifetime evaluation of catalyst performance.

4 Conclusions

This work systematically evaluated the catalytic performance of the DBD-DRM system and deeply

explored the effects of reaction parameters such as electric field intensity, gas flow rate, and temperature on the DRM reaction efficiency. Under the action of DBD, Ni-based catalysts showed excellent catalytic activity and carbon deposition resistance, and the catalytic performance was closely related to Ni particle size, dispersion, and metal-support interaction. The 20 wt % Ni@SiO_2 catalyst showed a higher conversion rate and product selectivity due to its larger pore size, higher pore volume, and excellent Ni particle dispersion. 20 wt % Ni@γ-Al_2O_3 showed better catalytic stability due to its strong metal-support interaction. The high-energy electrons and active free radicals generated by DBD effectively promoted the decomposition of CH_4 and CO_2 through vibrational excitation and direct collision. By constructing a nonequilibrium thermodynamic model, the energy distribution and competition mechanism of CH_4/CO_2 dry reforming in the DBD system were revealed. The high consistency between experimental data and theoretical predictions verified the reliability of the model. This work not only deepens the understanding of non-thermal plasma chemistry, but also provides technical support for the resource utilization of methane in the context of carbon neutrality.

Competing interests The authors declare that they have no competing interests.

Acknowledgements This work was supported by the China Scholarship Council (Grant No. 202306460067), the Beijing Natural Science Foundation (Grant No. 3232043), and the City University of Hong Kong Donation Research Grants (DON-RMG 9229021 and 9220061).

Electronic Supplementary Material Supplementary material is available in the online version of this article at https://doi.org/10.1007/s11705-025-2596-4 and is accessible for authorized users.

Funding Note Open access publishing enabled by City University of Hong Kong Library's agreement with Springer Nature.

References

1. Wang H, Diao Y, Gao Z, Smith K J, Guo X, Ma D, Shi C. H_2 production from methane reforming over molybdenum carbide catalysts: from surface properties and reaction mechanism to catalyst development. ACS Catalysis, 2022, 12(24): 15501–15528
2. Mohanty U S, Ali M, Azhar M R, Al-Yaseri A, Keshavarz A, Iglauer S. Current advances in syngas (CO + H_2) production through bi-reforming of methane using various catalysts: a review. International Journal of Hydrogen Energy, 2021, 46(65): 32809–32845
3. Yentekakis I V, Panagiotopoulou P, Artemakis G. A review of recent efforts to promote dry reforming of methane (DRM) to syngas production via bimetallic catalyst formulations. Applied Catalysis B: Environmental, 2021, 296: 120210
4. Yu J, Le T, Jing D, Stavitski E, Hunter N, Lalit K, Leshchev D, Resasco D E, Sargent E H, Wang B, et al. Balancing elementary steps enables coke-free dry reforming of methane. Nature Communications, 2023, 14(1): 7514
5. Zhu Q, Zhou H, Wang L, Wang L, Wang C, Wang H, Fang W, He M, Wu Q, Xiao F S. Enhanced CO_2 utilization in dry reforming of methane achieved through nickel-mediated hydrogen spillover in zeolite crystals. Nature Catalysis, 2022, 5(11): 1030–1037
6. Chan Y H, Chan Z P, Lock S S M, Yiin C L, Foong S Y, Wong M K, Ishak M A, Quek V C, Ge S, Lam S S. Thermal pyrolysis conversion of methane to hydrogen (H_2): a review on process parameters, reaction kinetics, and techno-economic analysis. Chinese Chemical Letters, 2024, 35(8): 109329
7. Yu K, Wang C, Zheng W, Vlachos D G. Dynamic electrification of dry reforming of methane with *in situ* catalyst regeneration. ACS Energy Letters, 2023, 8(2): 1050–1057
8. Nozaki T, Chen X, Kim D Y, Zhan C. Combination of DBD and catalysts for CH_4 and CO_2 conversion: basics and applications. Plasma Chemistry and Plasma Processing, 2023, 43(6): 1385–1410
9. García-Moncada N, Van Rooij G, Cents T, Lefferts L. Catalyst-assisted DBD plasma for coupling of methane: minimizing carbon-deposits by structured reactors. Catalysis Today, 2021, 369: 210–220
10. Aerts R, Martens T, Bogaerts A. Influence of vibrational states on CO_2 splitting by dielectric barrier discharges. Journal of Physical Chemistry C, 2012, 116(44): 23257–23273
11. Ray D, Nepak D, Janampelli S, Goshal P, Subrahmanyam C. Dry reforming of Methane in DBD plasma over Ni-based catalysts: influence of process conditions and support on performance and durability. Energy Technology, 2019, 7(4): 1801008
12. Wang H, Yang Y, Li Z, Kong X, Martin P, Cui G, Wang R. Plasma-assisted Ni catalysts: toward highly-efficient dry reforming of methane at low temperature. International Journal of Hydrogen Energy, 2023, 48(24): 8921–8931
13. Tu X, Whitehead J. Plasma-catalytic dry reforming of methane in an atmospheric dielectric barrier discharge: understanding the synergistic effect at low temperature. Applied Catalysis B: Environmental, 2012, 125: 439–448
14. Wang K, Ren X, Yin G, Hu E, Zhang H. Recent advances in plasma-based methane reforming for syngas production. Current Opinion in Green and Sustainable Chemistry, 2024, 50: 100981
15. Bogaerts A, Kozák T, Van Laer K, Snoeckx R. Plasma-based conversion of CO_2: current status and future challenges. Faraday Discussions, 2015, 183: 217–232
16. Snoeckx R, Bogaerts A. Plasma technology—a novel solution for

CO_2 conversion? Chemical Society Reviews, 2017, 46(19): 5805–5863

17. Snoeckx R, Zeng Y, Tu X, Bogaerts A. Plasma-based dry reforming: improving the conversion and energy efficiency in a dielectric barrier discharge. RSC Advances, 2015, 5(38): 29799–29808
18. Khoja A H, Mazhar A, Saleem F, Mehran M T, Naqvi S R, Anwar M, Shakir S, Saidina Amin N A, Sajid M B. Recent developments in catalyst synthesis using DBD plasma for reforming applications. International Journal of Hydrogen Energy, 2021, 46(29): 15367–15388
19. Li J Q, Bin X, Wang W B, Xie J J, Yin X L, Wu C Z, Xiao J B. Experimental study on dry reforming of methane by a plasma catalytic hybrid system. Journal of Fuel Chemistry & Technology, 2021, 49(8): 1161–1172
20. Uytdenhouwen Y, Hereijgers J, Breugelmans T, Cool P, Bogaerts A. How gas flow design can influence the performance of a DBD plasma reactor for dry reforming of methane. Chemical Engineering Journal, 2021, 405: 126618
21. Lu Q, Lei W, Yue W, Huang W, Dong Y, Yan W, Liu Y, Chen Y, Zhao Y. Reaction mechanism explorations on non-thermal plasma reforming of CO_2-CH_4 by combining kinetics modeling and emission spectroscopy measurements. Fuel, 2023, 344: 128041
22. Baig S, Sajjadi B. Non-thermal plasma enhanced catalytic conversion of methane into value added chemicals and fuels. Journal of Energy Chemistry, 2024, 97: 265–301
23. Sun J, Chen Q, Qin W, Wu H, Liu B, Li S, Bogaerts A. Plasma-catalytic dry reforming of CH_4: effects of plasma-generated species on the surface chemistry. Chemical Engineering Journal, 2024, 498: 155847
24. Arshad M Y, Saeed M A, Tahir M W, Pawlak-Kruczek H, Ahmad A S, Niedzwiecki L. Advancing sustainable decomposition of biomass tar model compound: machine learning, kinetic modeling, and experimental investigation in a non-thermal plasma dielectric barrier discharge reactor. Energies, 2023, 16(15): 5835
25. Sanjaya E, Weihs G F, Manaf N A, Abbas A. Reaction kinetic modelling of tar cracking in a non-thermal plasma reactor: model evaluation and reaction mechanism investigation. Chemical Engineering Journal, 2024, 479: 147649
26. Wang J, Zhang K, Bogaerts A, Meynen V. 3D porous catalysts for plasma-catalytic dry reforming of methane: how does the pore size affect the plasma-catalytic performance? Chemical Engineering Journal, 2023, 464: 142574
27. Miralai S, Monette E, Bartnikas R, Czeremuszkin G, Latreche M, Wertheimer M R. Electrical and optical diagnostics of dielectric barrier discharges (DBD) in He and N_2 for polymer treatment. Plasmas and Polymers, 2000, 5(2): 63–77
28. Chiper A S, Anița V, Agheorghiesei C, Pohoața V, Anița M, Popa G. Spectroscopic diagnostics for a DBD plasma in He/Air and He/N_2 gas mixtures. Plasma Processes and Polymers, 2004, 1(1): 57–62
29. Andersen J, Christensen J, Østberg M, Bogaerts A, Jensen A. Plasma-catalytic dry reforming of methane: screening of catalytic materials in a coaxial packed-bed DBD reactor. Chemical Engineering Journal, 2020, 397: 125519
30. Van Turnhout J, Aceto D, Travert A, Bazin P, Thibault-Starzyk F, Bogaerts A, Azzolina-Jury F. Observation of surface species in plasma-catalytic dry reforming of methane in a novel atmospheric pressure dielectric barrier discharge *in situ* IR cell. Catalysis Science & Technology, 2022, 12(22): 6676–6686
31. Wang B, Li X, Wang X, Zhang B. Effect of filling materials on CO_2 conversion with a dielectric barrier discharge reactor. Journal of Environmental Chemical Engineering, 2021, 9(6): 106370
32. Lü F C, Ruan H O, Song J X, Yin K, Zhan Z Y, Jiao Y F, Xie Q. Enhanced surface insulation and depressed dielectric constant for Al_2O_3/epoxy composites through plasma fluorination of filler. Journal of Physics D: Applied Physics, 2019, 52(15): 155201
33. Jiang N, Qu Y, Zhu J, Wang H, Li J, Shu Y, Cui Y, Tan Y, Peng B, Li J. Remediation of atrazine-contaminated soil in a fluidized-bed DBD plasma reactor. Chemical Engineering Journal, 2023, 464: 142467
34. Chi J, Wu X, Tao J, Min X, Li Z, Zhao S. DBD-coupled highly dispersed Ni/SiO_2 materials for CO_2 reduction performance and mechanism study. Journal of the Energy Institute, 2024, 113: 101552
35. Mei D, Tu X. Atmospheric pressure non-thermal plasma activation of CO_2 in a packed-bed dielectric barrier discharge reactor. ChemPhysChem, 2017, 18(22): 3253–3259
36. Zhang K, Zhang G, Liu X, Phan A N, Luo K. A study on CO_2 decomposition to CO and O_2 by the combination of catalysis and dielectric-barrier discharges at low temperatures and ambient pressure. Industrial & Engineering Chemistry Research, 2017, 56(12): 3204–3216
37. Sivachandiran L, Da Costa P, Khacef A. CO_2 reforming in CH_4 over Ni/γ-Al_2O_3 nano catalyst: effect of cold plasma surface discharge. Applied Surface Science, 2020, 501: 144175

Electronic Supplementary Material

Non-thermal plasma driven dry reforming of methane: electron energy-input power coupling mechanism and catalyst design criteria

Minghai Shen[1,3], Wei Guo[1], Lige Tong (✉)[1], Li Wang[1], Paul K. Chu (✉)[2], Sibudjing Kawi (✉)[3], Yulong Ding (✉)[4]

1 School of Energy and Environmental Engineering, University of Science and Technology Beijing, Beijing 100083, China

2 Department of Physics, Department of Materials Science and Engineering, and Department of Biomedical Engineering, City University of Hong Kong, Hong Kong, China

3 Department of Chemical and Biomolecular Engineering, National University of Singapore, Singapore 119260, Singapore

4 Birmingham Centre for Energy Storage & School of Chemical Engineering, University of Birmingham, B15 2TT, UK

E-mails: tonglige@me.ustb.edu.cn (Tong L); paul.chu@cityu.edu.hk (Chu P K); chekawis@nus.edu.sg (Kawi S); Y.Ding@bham.ac.uk (Ding Y)

Table of Contents

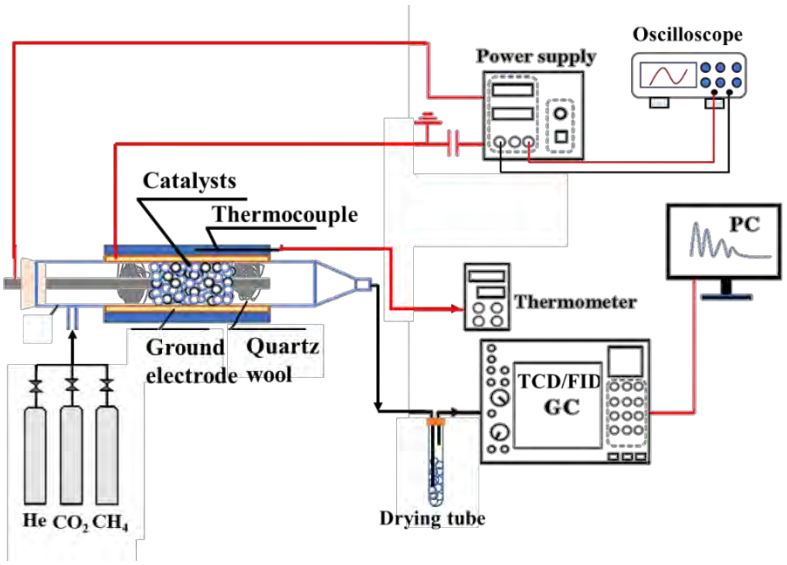

Supplementary Fig.1. Schematic diagram of the cylindrical DBD reactor system.

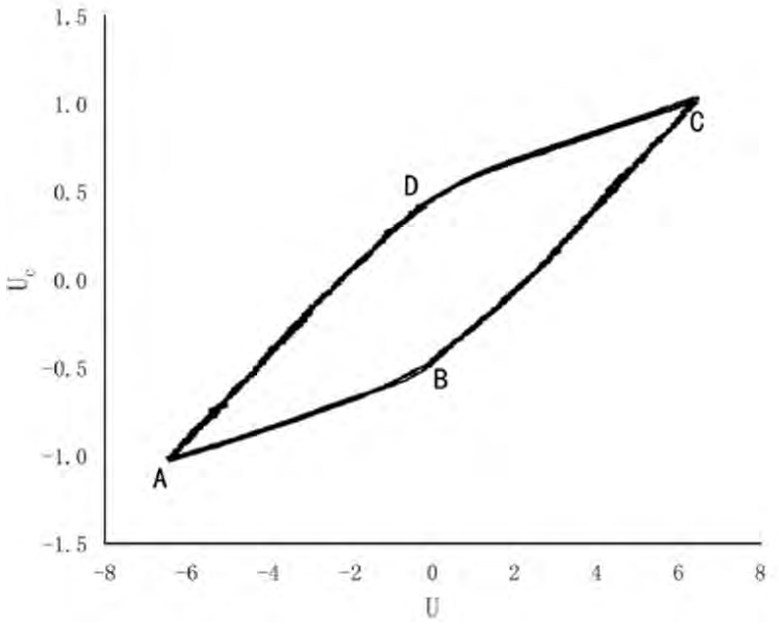

Supplementary Fig. 2. Typical DBD Lissajous figures.

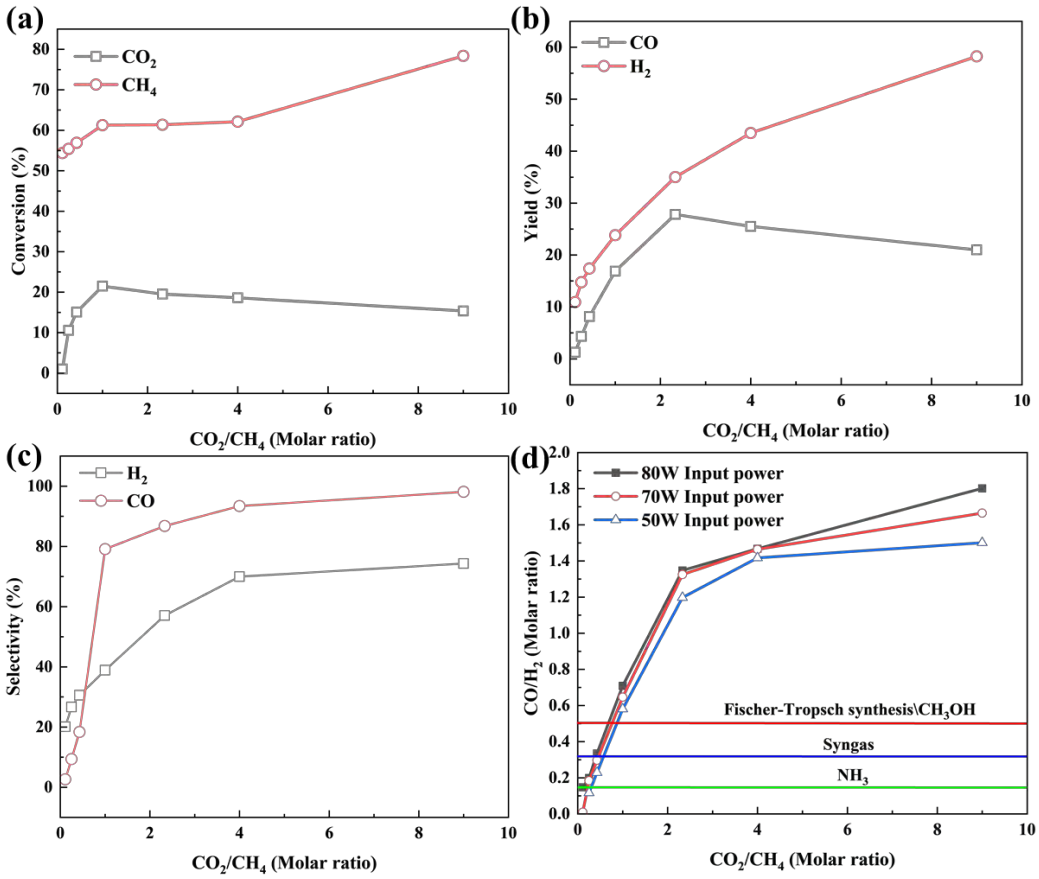

Supplementary Fig. 3. Comparison of CO and H_2 production performance at different CO_2/CH_4 feed molar ratios (total gas flow = 30 mL/min). (a) Selectivity of H_2 and CO. (b) Yields of H_2 and CO. (c) Conversion of CH_4 and CO_2 feedstocks. (d) Product CO/H_2 molar ratio.

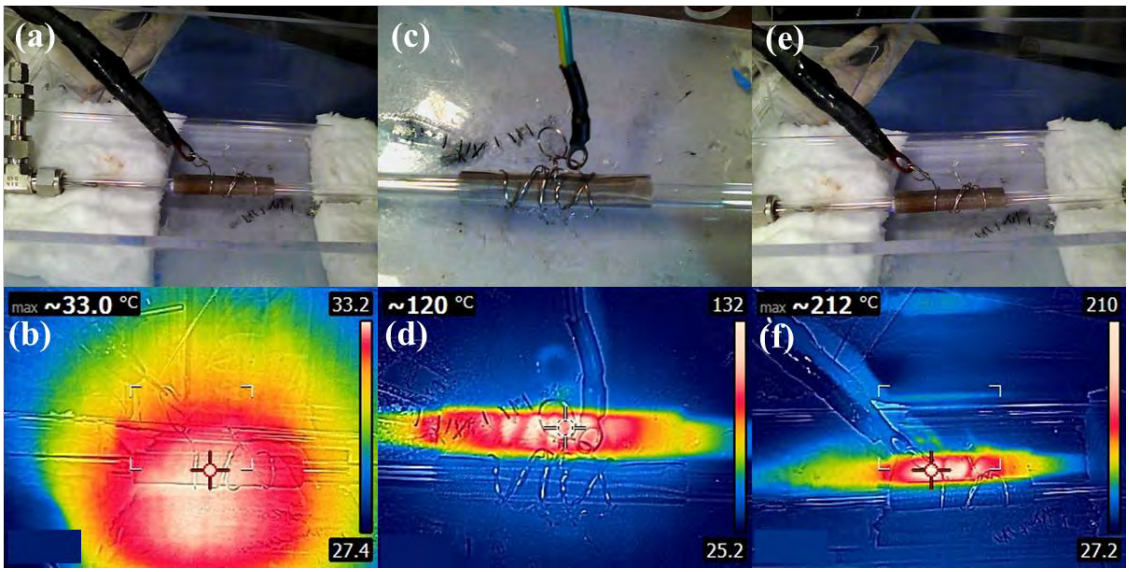

Supplementary Fig. 4. Schematic diagram of the infrared thermal imaging temperature of small reactors with different input powers: (a and b) 40 W; (c and d) are 60 W; (e and f) 100 W.

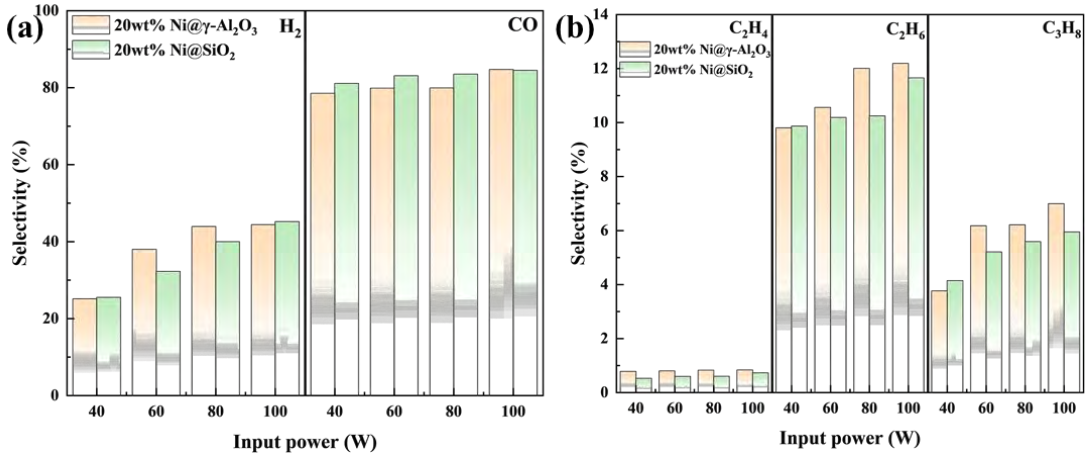

Supplementary Fig. 5. Selectivity of Ni-based catalysts at different input powers: (a) H_2 and CO; (b) C_2H_4, C_2H_6 and $C3H_8$.